The Role of Mesoscopic PCBM Crystallites in Solvent Vapor Annealed Copolymer Solar Cells

Tricia A. Bull,[†] Liam S. C. Pingree,[‡] Samson A. Jenekhe,[‡,§,*] David S. Ginger,[‡] and Christine K. Luscombe[†,*]

[†]Department of Materials Science & Engineering, University of Washington, Box 352120, Seattle, Washington 98195-2120, [‡]Department of Chemistry, University of Washington, Box 351700, Seattle, Washington 98195-1700, and [§]Department of Chemical Engineering, University of Washington, Box 351750, Seattle, Washington 98195-1750

ABSTRACT Solution processable methanofullerene-based solar cells are the most widely studied class of organic photovoltaics (OPVs). The evolution of the electronic properties with solvent vapor annealing (SVA) in polyfluorene-copolymer and [6,6]phenyl-C61-butyric acid methyl ester (PCBM) blended OPVs is studied using various scanning probe techniques: light beam induced current spectroscopy (LBIC), conductive atomic force microscopy (c-AFM), and photoconductive AFM (pc-AFM). We demonstrate that SVA improves the power conversion efficiency by 40% while forming mesoscopic PCBM crystallites and a ~3 nm copolymer-rich overlayer at the cathode interface. We find that the large crystallites created during annealing do not directly improve the local performance of the device, but instead attribute the performance improvement to the ripened blend morphology and an increase in the hole mobility of the copolymer in comparison to the unannealed blend. The PCBM-rich aggregates act as a sink for excess PCBM, although excess PCBM is initially required to form the appropriate structural features prior to the annealing process.

KEYWORDS: organic photovoltaic · solar cell · PCBM · solvent vapor annealing · photoconductive atomic force microscopy · light beam induced current microscopy

The highest efficiency organic photovoltaics to date rely on thermal and/or vapor annealing, which induces polymer reordering and PCBM ([6,6]phenyl-C61-butyric acid methyl ester) crystallization.[1,2] The role of polymer rearrangement is at least partly understood, yet there are many conflicting explanations for the effect that PCBM crystallites have on charge separation and conduction.[3−7] In this paper, we experimentally examine the role of mesoscopic PCBM crystallites in a fluorene-based copolymer/PCBM blend by using multiscale characterization techniques to spatially correlate device performance with morphology.

The demand for affordable solar technologies has led to the development of organic photovoltaics (OPVs).[8−10] The most efficient solution processable OPVs to date utilize the bulk heterojunction architecture, where typically a blend of a conjugated donor polymer and an acceptor fullerene is sandwiched between two electrodes.[11] Since light absorption in organic semiconductors primarily produces bound excitons, a high density of donor−acceptor heterointerfaces is needed due to the relatively small exciton diffusion length (~10 nm).[12] Beyond facilitating exciton dissociation, the blend structure needs to provide separate conduction pathways for electrons and holes to promote efficient transport and limit recombination. To date, the power conversion efficiency (PCE) of the best organic solar cells has reached 5−6%.[13,14] This efficiency is limited by poor overlap of the polymer's absorption with the solar spectrum, recombination and/or trapping, low open circuit voltages, and low fill factors in various donor−acceptor blends.[8,15,16] While an ideal material system and blend structure have not yet been realized, efforts to increase the efficiency in OPVs are currently focusing on the selection of high mobility, broadly absorbing donor polymers, and the manipulation of the donor−acceptor blend morphology through various annealing processes.[17−20]

A variety of low band gap donor−acceptor (D−A) copolymers have been developed for PCBM-based OPVs since they are capable of absorbing more of the solar spectrum compared to the most efficient and well-studied donor polymer, poly(3-hexylthiophene) (P3HT).[21−25] The advantage of D−A copolymers is that the degree of intramolecular charge transfer between the donor and acceptor moieties can be tuned to achieve targeted optical and electronic properties. In this study, we explore the photovoltaic behavior of a D−A copolymer, poly(5,7-bis(3-dodecylthiophen-2-yl)thieno[3,4-*b*]pyrazine-*alt*-9,9-dioctyl-2,7-fluorene) (BTTP-F), previously reported

*Address correspondence to luscombe@u.washington.edu, jenekhe@u.washington.edu.

Received for review December 21, 2008 and accepted February 08, 2009.

10.1021/nn800878c CCC: $40.75

by Zhu and Jenekhe,[26] blended with PCBM. This copolymer is a good OPV donor candidate because it has a high field-effect hole mobility of 1.6×10^{-3} $cm^2/V \cdot s$, has two broad absorption bands at 670 and 420 nm, and has a stable HOMO level of 5.0 eV.

Although the electronic properties of the fluorene–thienopyrazine copolymer, BTTP-F, make it an attractive donor polymer, the morphology of the components must still be optimized to achieve the best efficiency in any blend system. Relative PCE improvements of 100% have been achieved in P3HT/PCBM OPVs *via* thermal annealing, vapor annealing, and a combination of both.[1,27,28] In our fluorene–thienopyrazine copolymer/PCBM system, we use solvent vapor annealing of the films to increase the device performance and observe the resultant formation of mesoscopic crystalline PCBM aggregates, or crystallites. PCBM aggregates ranging in size of 10–100 μm have been observed in various polymer/PCBM blends.[5−7,29] Nilsson demonstrated that in fluorene-based copolymer/PCBM systems the solvent evaporation rate and the PCBM solubility limit determine the stability of the blend; fast evaporation results in metastable spinodal decomposition, whereas slow evaporation allows time for PCBM crystallization.[30] While it is agreed that PCBM crystallite formation depends on diffusion,[31] the effects of the different sized aggregates that form during the annealing process are still not fully understood in the most-studied P3HT/PCBM system, let alone in other polymer/fullerene blends.

Intuitively, the formation of micron-scale PCBM crystallites, as is sometimes observed, seems unlikely to improve the performance of any OPV. Large crystallites should not contain the nanoscale interfacial area required for efficient exciton harvesting. However, many studies have reported improved short-circuit currents in OPVs containing relatively large (50 nm to 50 μm) crystalline aggregates and even 300 μm spherulites.[4−6] Researchers have proposed that the photoconductivity is enhanced around the PCBM aggregates in MDMO-PPV/PCBM solar cells, and a larger volume of the enhanced region leads to greater photocurrents (*i.e.*, blends with 20 nm aggregates had higher photocurrents than blends with 200 nm aggregates).[6,7] The authors attributed the photoconductivity increase to less geminate recombination as a result of electron diffusion to the PCBM aggregates and hence longer electron lifetimes. They also proposed that the electron mobility is enhanced within the PCBM aggregates. In contrast, in MEH-PPV/PCBM blends, results from near-field scanning photocurrent microscopy (NSPM) have suggested that no photocurrent amplification in the PCBM depletion region surrounding the PCBM aggregate occurs; rather, the photocurrent enhancement is attributed to an increase in the hole mobility of the polymer.[5] Other research has shown vertical phase segregation of PCBM toward the anode is reduced during annealing, resulting in an increase in the solar cell's shunt resistance.[32] As evident from these observations, multiple processes have been credited to improved power conversion efficiencies in polymer/PCBM blends containing PCBM aggregates. In summary, these processes include (1) improved charge dissociation, (2) an increase in the lifetime of the charge carriers surrounding the PCBM crystallites, (3) enhanced electron mobility in the PCBM crystallites, (4) an increase in the hole mobility in the polymer/PCBM matrix, and (5) an increase in the shunt resistance due to vertical phase separation. It is unclear whether or not the increase in device efficiency is a result of all or a combination of these effects.

In this paper, we examine the role of PCBM crystallites in BTTP-F/PCBM solar cells using a combination of characterization tools to study the electronic properties on a wide range of length scales as a function of annealing. It is known that the relevant length scales for exciton diffusion and charge transport are ~10 and ~150 nm (depending on device thickness), respectively. Nevertheless, annealed devices that exhibit improved performance relative to unannealed devices are shown to contain PCBM crystallites that can be 20–150 μm in diameter. In order to better understand the role played by the annealing process and the large PCBM crystallites, we apply a modified scanning light beam induced current (LBIC)[33−37] technique, conductive atomic force microscopy (c-AFM),[38−46] and photoconductive atomic force microscopy (pc-AFM)[47] to determine the local variations in cell performance before and after solvent annealing with 20 nm resolution.

RESULTS AND DISCUSSION

Device Characteristics. BTTP-F/PCBM bulk heterojunction solar cells were fabricated with various concentrations of PCBM and solvent vapor annealing (SVA) times. The primary observation is that SVA dramatically enhances the device performance. Figure 1A shows the photovoltaic output of an average cell with an optimized blend composition (83 wt % PCBM) before and after SVA. Following SVA, the short-circuit current increased by 30%, the fill factor (FF) increased from 0.43 to 0.51, and the shunt resistance increased, resulting in a 45% increase in the power conversion efficiency (PCE). The best devices achieved a 1.4% PCE. Spectral mismatch correction factors were 1.02 for the unannealed and annealed devices.[48] Thermal annealing of the as-spun films at 120 °C for 30 min produced no observable effect on the PCE.

Figure 1B shows the PCE and the FF of the unannealed devices and the PCE of the annealed devices, before and after SVA as a function of PCBM concentration. On average, the PCE increased by 40–50% after treatment with solvent vapor for 1 h regardless of the PCBM concentration. However, the FF of the annealed blend increased with PCBM loading, where the PCE correlated positively with the FF until reaching a PCBM

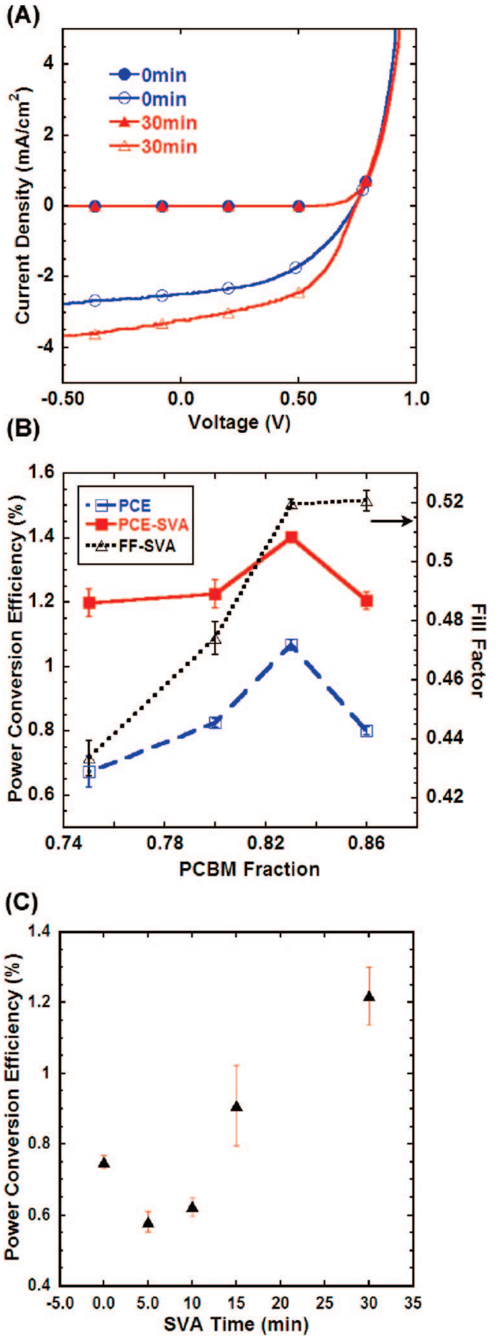

Figure 1. (A) Average *I*−*V* characteristics before (0 min) and after 30 min of SVA BTTP-F/PCBM solar cells containing 83% PCBM by weight. (B) PCE *versus* PCBM concentration before and after 1 h of SVA, and FF *versus* PCBM concentration of unannealed devices. (C) PCE *versus* SVA time in 83% PCBM devices shows an initial decrease in efficiency than increased efficiency after 15 min of SVA.

fraction of 0.83. This trend correlates well with the observation that increasing fractions of PCBM well beyond the percolation threshold in polyfluorene/PCBM blends results in higher carrier mobilities.[49] The decrease in efficiency at greater PCBM concentrations is likely caused by polymer absorption losses or formation of more discontinuous hole conduction pathways.

Figure 1C shows the performance of a series of 83% PCBM blends as a function of SVA time. We find that exposure to solvent vapor for 30 min is the optimum annealing time for the blend. However, the device performance degrades during the first 5−10 min of annealing, which suggests that the initial restructuring that takes place in the film is actually detrimental to device performance. Optical inspection of these annealed films with increasing SVA time indicates a restructuring of the blend on several length scales as shown in Figure 2. Unannealed films show no structural features, but an underlying structure emerges after ~5 min of annealing. After 10 min, visible 50 μm aggregates form, and after 30 min, the aggregate diameters can reach 200 μm. TEM and grazing-angle XRD clearly indicate that the aggregates are crystalline and PCBM-rich with *d* spacings of 0.3 nm (Figures S1 and S2 in the Supporting Information), which match literature values for pristine PCBM.[50,51]

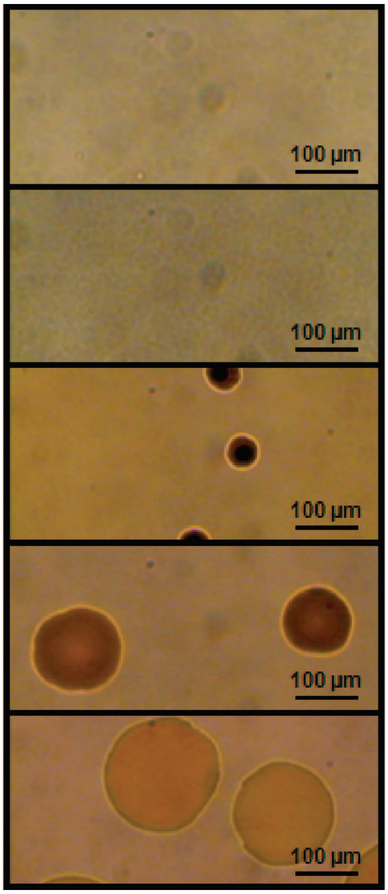

Figure 2. Optical images of BTTP-F/PCBM blend films (83% PCBM) after 0, 5, 10, 15, and 30 min (from top to bottom) of SVA. Films correspond to devices measured in Figure 1C. After 5 min of SVA, a ripened structure emerges, and after 10 min, PCBM crystallites form and ripen with increasing SVA time.

Optical Properties. Figure 3 shows the absorbance spectra of the blend films on PEDOT:PSS/ITO/glass substrates with increasing annealing time. There are both a red shift of BTTP-F's 610 nm absorption peak and an increase in overall absorbance with increasing SVA time. After 5 min of SVA, the absorption peak of BTTP-F

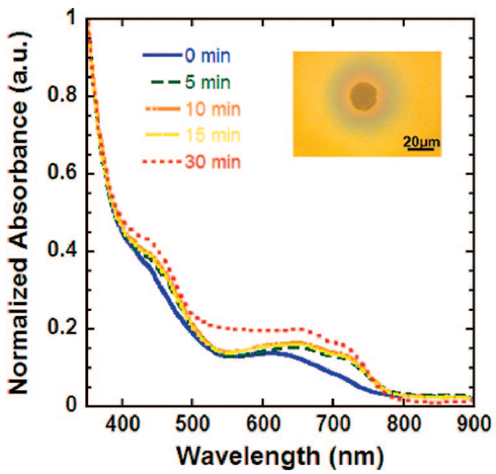

Figure 3. Absorption of BTTP-F/PCBM blends (83% PCBM) on PEDOT-PSS/glass substrates after 0, 5, 10, 15, and 30 min of SVA. The BTTP-F absorption peak red shifts after 5 min of SVA, and the blend's absorbance increases after 10 min. Inset shows the optical image of PCBM crystallite after 30 min of SVA.

red shifts 40 nm and there is a small absorbance increase at 650 nm of 0.03. No red shift occurs after 30 min of annealing, but there is an additional 0.5 increase in the absorbance at 650 nm. This red shift at small annealing times suggests an initial BTTP-F reordering, while the absorbance increase after 30 min of annealing indicates longer range molecular rearrangement, as evidenced by the emergence of more structure in the absorption band around 720 nm.

The peak external quantum efficiency (EQE) of the annealed BTTP-F/PCBM solar cell also red shifts in comparison to the unannealed device (S4). Integration of the EQE spectrum reveals a 9% decrease in the EQE following SVA in contrast to the increase in PCE. The calculated J_{sc} values (integration of the product of the EQE and AM 1.5 solar spectrum) of the unannealed and annealed devices were 3.2 and 3.7 mA/cm^2, corresponding to an 8 and 24% underestimate of the J_{sc} in comparison to those values measured under the standard solar spectrum at 1 Sun. We have excluded any spectral mismatch errors since the mismatch factors were nearly unity for both the unannealed and annealed devices. In the annealed devices, we suspect scattering from the crystallites during the PCE measurement to account for the overall increase in the measured J_{sc}. The bright field transmission inset in Figure 3 supports this hypothesis, where lensing can be seen around a crystallite.

Light Beam Induced Current Microscopy (LBIC). To better understand the effect of the crystallites on device performance, LBIC was used to study photocurrent distributions in films both before and after SVA. LBIC microscopy involves scanning a tightly focused laser spot across the device and recording the photocurrent distribution. Figure 4 shows maps of the annealed and unannealed blends, as well as *IV* curves at specific points in the film. Figure 4c shows nearly uniform photocurrents in the unannealed devices, with currents ranging between 1.7 and 1.8 nA at an incident laser power (prior to entering the microscope) of 2 mW. At points D and E, the *IV* characteristics are identical and the short-circuit currents are 1.8 nA, in good agreement with the LBIC map. The uniform currents can be attributed to fairly uniform mixing of both the BTTP-F and PCBM constituents on optical length scales. In contrast, Figure 4a shows that the annealed films exhibit substantial spatial variations in the photocurrent, with significant reductions in the current on top of the large PCBM crystallite and some photocurrent enhancement in a small ~10 μm diameter region surrounding the PCBM crystallite.

At identical laser powers, the current observed on the PCBM crystallite is lower than that observed in the unannealed device, while the photocurrent recorded away from the PCBM crystallites is higher than that observed in the unannealed films. Measured with LBIC, the overall photocurrent increase following annealing is consistent with the bulk device behavior as there is a 50% overall increase in the I_{SC}. However, as expected, the PCBM crystallite is barely photoactive. Instead, a ~10 μm enhanced region surrounds the crystallite, and

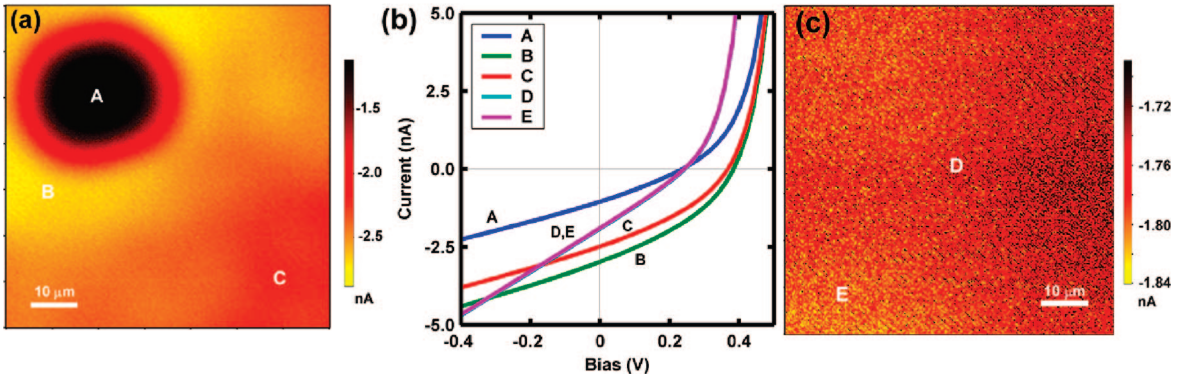

Figure 4. (a) LBIC map of 30 min SVA 1:5 BTTP-F/PCBM film with a large PCBM crystallite. The PCBM crystallite does not generate large photocurrents, but a region surrounding the crystallite is enhanced. (b) *I*—*V* characteristics corresponding to locations on panels a and c. The crystallite (A) produces the smallest power followed by the unannealed blend (D,E), but the enhanced region in the annealed blend (B) and the matrix (C) produce the greatest power. (c) LBIC map of the unannealed blend showing uniform photocurrent generation.

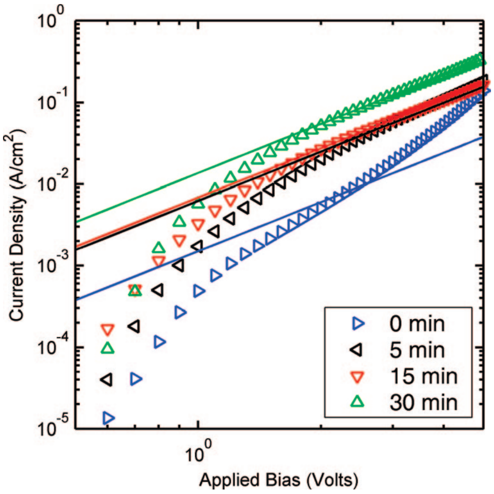

Figure 5. Log J−log V plot showing dark current of hole-only devices after 0, 5, 15, and 30 min of SVA. The SCLC hole mobility increases with annealing time, as calculated from the Mott-Gurney law (the linear lines corresponds to a slope = 2). The unannealed blend does not show SCLC transport and is instead trap-limited.

a greater average photocurrent is measured in the matrix compared to the unannealed blend. The I_{SC} of the crystallite is only 1 nA, the matrix is 2.5 nA, and the area immediately surrounding the crystallite is 3.0 nA (Figure 4b). The region surrounding the crystallite has nearly double the photocurrent of the unannealed blend. This result is in contrast to the behavior reported for 10−20 μm PCBM aggregates in the MEH-PPV/PCBM system, where current-depleted regions were observed surrounding the crystallites.[5]

Interestingly, the enhanced photoactive region in Figure 4 compares with the green halo region observed around the crystallite in Figure 3. Photocurrent is likely improved close to the PCBM crystallites due to increased light absorption in this region.

Charge Transport and Conductive AFM (c-AFM). Annealing has been reported to increase hole mobility in a number of polymer blends.[52−54] We used space charge limited current (SCLC) measurements to measure the effective hole mobility as a function of annealing time in our devices.[55,56] Comparison of the dark currents between the unannealed and the 30 min annealed devices shows that the hole dark current is increased by nearly an order of magnitude (Figure 5), indicating better hole transport in the annealed blend. While the annealed film exhibits the expected dependence of current density on V^2, as predicted by the Mott-Gurney law, the unannealed film does not, preventing a direct comparison of mobilities between the annealed and unannealed film.[57] However, these results suggest that annealed films possess improved order and lower trap densities. After only 5 min of SVA, we begin to observe SCLC transport. Additional annealing beyond 5 min continues to improve transport: the SCLC hole mobility increases by a factor of 5 from 9.56×10^{-5} cm^2/V·s after 5 min of SVA to 2.17×10^{-4} cm^2/V·s after 30 min of SVA. This is comparable to the SCLC hole mobility of 2×10^{-4} cm^2/V·s measured in MDMO-PPV/PCBM blends.[58]

To examine the evolution of hole mobility with annealing time, c-AFM was used to simultaneously map both the surface morphology and the current passing through the tip−sample junction, thus providing a qualitative map of charge transport. While it is possible to make quantitative mobility measurements with c-AFM,[46] doing so requires careful attention to the details of the barrier to charge injection from the tip and sample−tip interactions. Nevertheless, c-AFM can easily be used to qualitatively map the dominant hole and electron transport pathways at the film surface.

Figure 6 shows c-AFM dark current maps under forward bias and reverse bias both before and after SVA. In this paper, we refer to forward bias when the ITO contact is biased positive, regardless of whether the cathode is an evaporated metal contact in a device, or a Pt-coated c-AFM tip. Thus, under reverse bias, holes are injected from the sharp tip, and the c-AFM images show the most current where hole injection and transport are prevalent. Likewise, under forward bias, electrons will be injected through the tip, and the forward bias c-AFM images thus show more current where the sample is PCBM-rich. Comparison of forward and reverse bias images can thus be used to differentiate between local composition as well as provide information about the transport networks.[59] In contrast to the optical images, the atomic force microscopy images reveal distinct nanoscale phase separation of PCBM-rich phases and BTTP-F-rich phases in both the annealed and unannealed devices. In reverse bias, the “valley” regions in the morphology correlate primarily with the hole conduction pathways (Figure 6a,b). In forward bias, the taller regions are preferentially electron-conducting pathways.

As the film is annealed in solvent vapor, the average morphology ripens, resulting in domain sizes 200−400 nm wide and 20 nm tall (Figure 6d). In reverse bias (so the holes are injected from the tip), the hole current map still correlates preferentially to the lower regions on the sample. Regardless, the maximum magnitude of the current transported in the annealed blend is 100 pA and only 20 pA in the unannealed film (Figure 6b,e). This 5-fold increase in the current agrees with the increased SCLC hole mobility. We can thus attribute the hole mobility increase to the ripened domains.

In forward bias, the current maps of the annealed sample show less direct correlation with the film topography. While the electron current increases after annealing, the active domains are small and discontinuous. Comparison of the two maps in both forward and reverse bias shows electrically inactive regions within the annealed film. Regardless of the bias, part of the device is rectifying the current. We attribute this to verti-

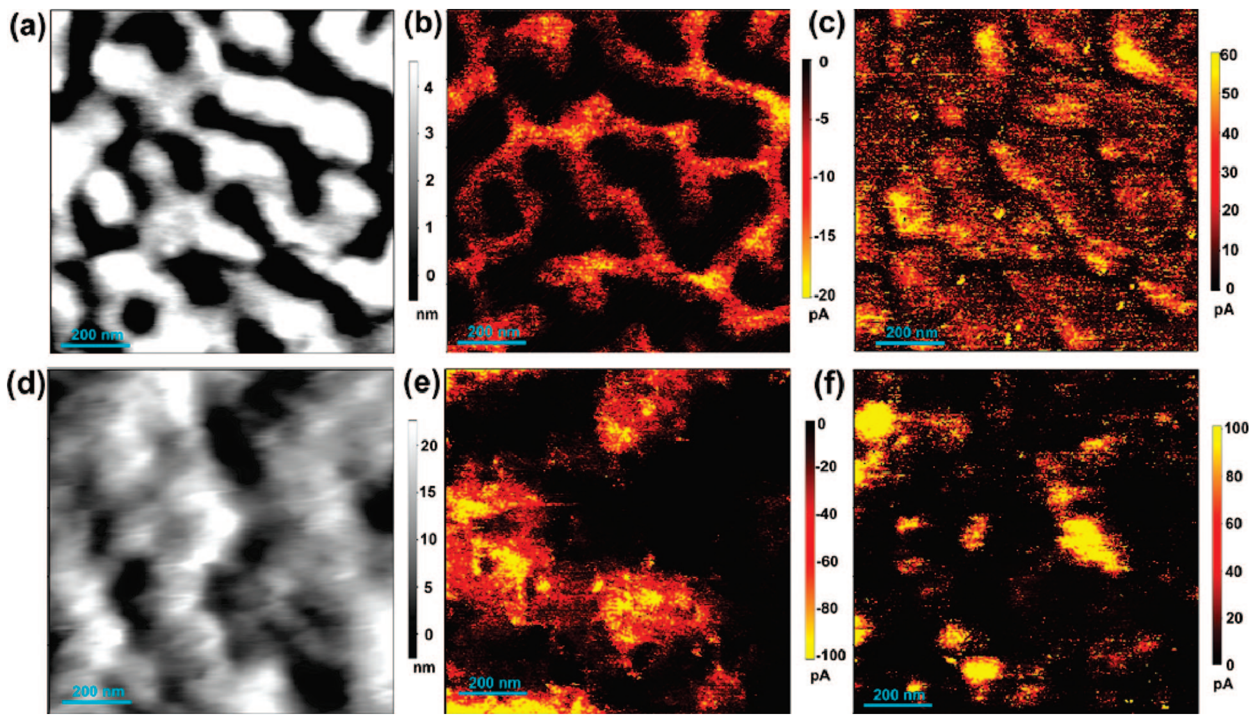

Figure 6. AFM topography of unannealed BTTP-F/PCBM blend (a) and corresponding c-AFM maps at −8 V (b) and +8 V (c). Bulk blend topography after 30 min of SVA is shown in (d) with corresponding c-AFM at −8 V (e) and +8 V (f). Active regions in reverse bias correspond to hole conduction pathways, and active regions in forward bias correspond to electron conduction pathways.

cal phase separation and the formation of a BTTP-F-rich surface layer, which creates effective p−n−p junctions in some regions within the device, thus limiting charge injection/extraction by the AFM tip.[45] We confirmed these changes in near-surface vertical morphology by using XPS, as described below.

Angle-Resolved X-ray Photoelectron Spectroscopy (XPS). The c-AFM data suggest that the composition near the film surface may evolve during SVA. To test this hypothesis, we performed angle-resolved XPS on the annealed and unannealed films. Figure 7 shows the composition of sulfur and nitrogen in the annealed and unannealed blends, which are unique elements to BTTP-F not present in the PCBM. The composition of S and N goes to zero at 4 nm because the compositional resolution is limited by the sampling angle and signal intensity.[60] In both films, there is a surface-rich layer of BTTP-F, which is consistent with a previous study that indicates vertical phase segregation of as-spun fluorene-based copolymer/PCBM blends.[61] Comparison of the sulfur and nitrogen content in the annealed blend shows that the BTTP-F-rich surface layer is 10 Å closer to the air interface than in the unannealed blend. In the unannealed film, the S and N concentration decreases 38−39 Å from the air interface, whereas the S and N in the annealed blend is concentrated to the first 25−32 Å of the film surface. While the relative concentrations of the BTTP-F at the surface cannot be precisely determined because the surface roughness of the annealed blend is not considered in the model, it is clear that the annealed film contains more BTTP-F at the surface than the unannealed blend (Table S1 in the Supporting Information).

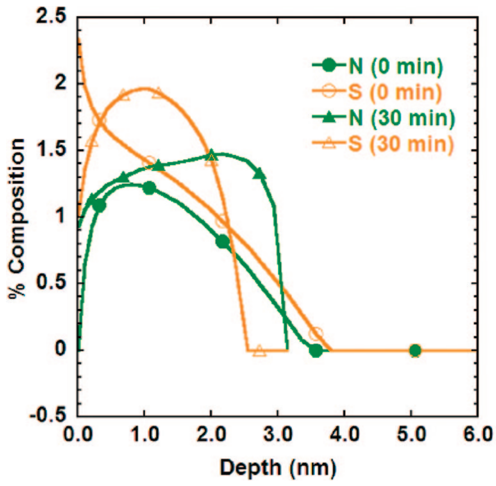

Figure 7. Angle-resolved XPS depth profile of sulfur and nitrogen in 1:5 BTTP-F/PCBM blend before annealing and after 30 min of SVA. Depth of 0 corresponds to the air/blend interface.

Photoconductive AFM (pc-AFM). The interplay of a three-tier system consisting of a matrix of PCBM and BTTP-F, ripened PCBM-rich domains and crystallites, and a thin copolymer overlay is further examined using photoconductive AFM (Figure 8). We expect the near-surface BTTP-F layer to limit short-circuit currents by limiting the extraction of electrons through the pc-AFM tip. This expectation seems to be confirmed by the localized regions of photocurrent seen in Figure 8e, whereas the unannealed film shows larger apparent areas of photo-

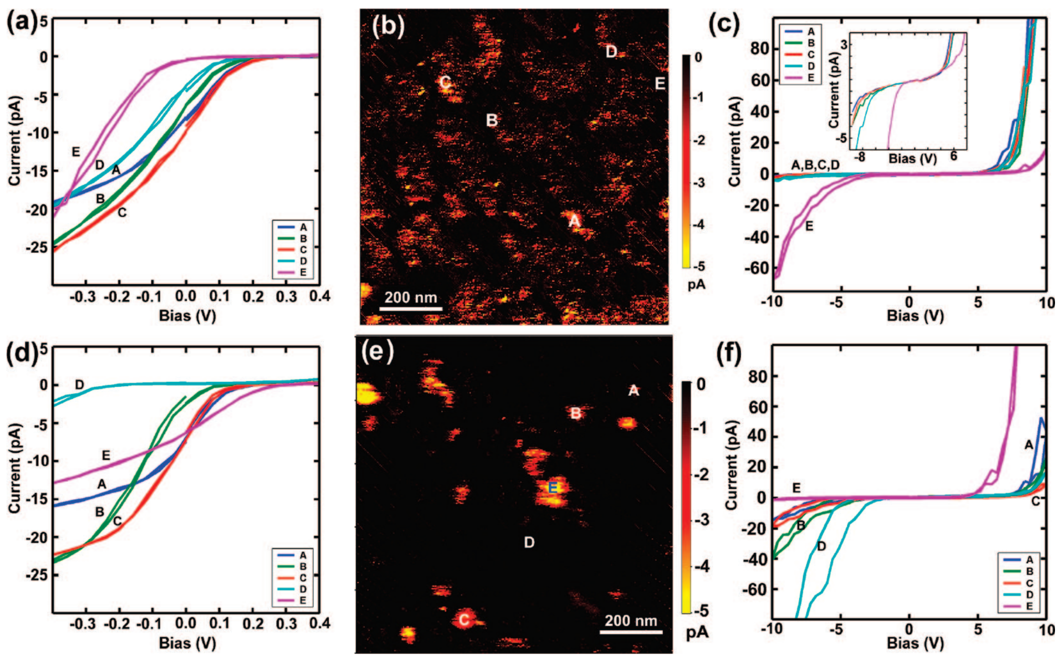

Figure 8. Unannealed film: (a) *IV* characteristics under 2 mW, 632 nm laser with Pt AFM tip, (b) pc-AFM short circuit map, and (c) dark *IV* curves. Annealed film: (d) illuminated *IV* characteristics, (e) pc-AFM short-circuit map, and (f) dark *IV* curves.

current generation. However, the upper photocurrent values are nearly doubled in the annealed film (~4−5 pA range in the annealed film compared to a 2−4 pA range in the unannealed film).

Quantitative comparison of the pc-AFM images of the two samples is restricted by the change in near-surface film composition. Since the device performance increases, we do not expect decreased photocurrents with pc-AFM. Indeed, the *IV* curves obtained from the LBIC technique, where thermally evaporated contacts are used for charge extraction, show increased local photocurrents after annealing. Nevertheless, the *IV* curves obtained from the pc-AFM and LBIC measurements seem consistent in many aspects. For instance, regions generating photocurrent in the pc-AFM maps have a higher V_{OC} and I_{SC} than the dark regions, which is consistent with the LBIC *IV* characteristics (Figure 4b). The regions with greater I_{SC} tend to have greater forward bias dark currents (Figure 8c,f). This dark and light *IV* correlation is consistent since forward currents are associated with electron injection, and good electron extraction at the tip is required for a greater I_{SC}. As such, regions with low photocurrents have a high hole mobility, for example, point E in the unannealed sample and point A in the annealed sample. This trend is further demonstrated by the inset in Figure 8c. Maps were also taken on top of several crystallites that show little photocurrent and smaller dark currents than the annealed matrix (Figures S8 and S13 in the Supporting Information). Thus, the best performance on the film surface is related to areas with high forward bias dark currents and/or better electron conduction (injection/extraction). The poorly performing regions correspond to a BTTP-F-rich surface that has high reverse bias dark currents and poor electron extraction.

To overcome the barrier to electron extraction as a result of the insulating BTTP-F overlayer, we acquired bias-dependent imaging under illumination. Images from pc-AFM were collected at −0.5 and −1 V to show where the photoactive short-circuit regions are emerg-

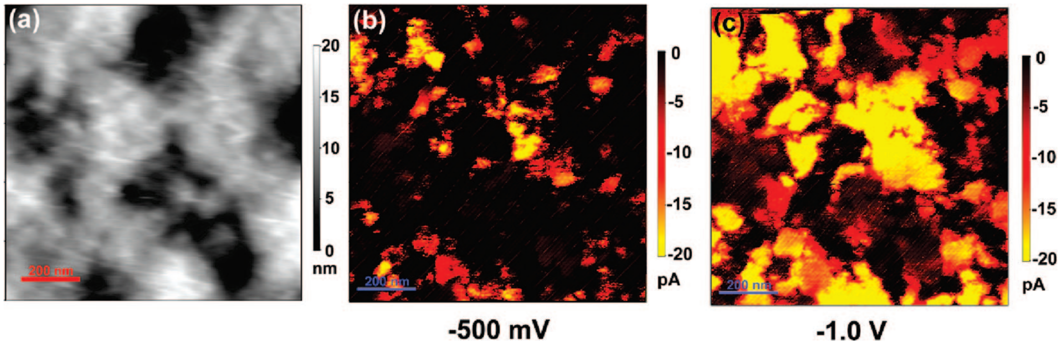

Figure 9. (a) AFM of unannealed blend and corresponding (b) pc-AFM at −0.5 V, (c) pc-AFM at −1.0 V; (d) AFM of annealed blend and corresponding (e) pc-AFM at −0.5 V, (c) pc-AFM at −1.0 V.

ing in the annealed films (Figure 9). Complete bias-dependent images of annealed and unannealed films are provided in Figures S11−S13 in the Supporting Information. It is important to remember that, in this regime, the magnitude of the current on pc-AFM maps is not in direct proportion to the power produced by the device.

Topographical images of the annealed blend show an increase in the active domain size with increasing negative bias (Figure 9b,c). This suggests the barrier to charge extraction caused by the BTTP-F overlayer is surmounted at −1 V. Closer examination of the annealed film at −1 V demonstrates the interconnectivity of the ripened domains. While the polymer overlayer limits charge extraction, the small bias required to overcome this suggests that this physical barrier is likely not severely limiting device performance. Yet, removal of the overlayer or disruption/penetration during cathode deposition would still be advantageous for improved electron extraction.

CONCLUSIONS

Treating BTTP-F/PCBM solar cells with solvent vapor results in both the formation of mesoscopic PCBM crystallites, ripening of electron-transporting domains, as well as the formation of a copolymer-rich overlay. At the same time, in spite of the unfavorable change in the vertical film morphology we detected by c-AFM and XPS, and the formation of the very large PCBM crystallites, the power conversion efficiency of the devices increases by 40%. Correlation of morphology with the local electrical properties at characteristic length scales from 100 nm to tens of microns was made possible by combining LBIC, c-AFM, and pc-AFM. While the large crystallites do not directly improve device efficiency or transport, they are associated with surrounding regions of increased light absorption and improved photocurrent. The main source of the improved photocurrent following annealing is improvement in local charge transport pathways and polymer packing and the resultant increase in hole mobility.

These hierarchical structures and their interactions help us better understand the role of varying degrees of phase separation in methanofullerene-based solar cells. The enhanced photocurrents in the annealed film regions that show increased polymer absorption suggests that the large PCBM crystallites may merely be acting as sinks for excess PCBM in the film. If so, finding ways to nucleate the desired local film morphology during annealing (such as with surface chemistry)[62−64] without having to include such large fractions of PCBM could lead to further increases in device performance. Although they form during annealing, neither the very large mesoscopic PCBM crystallites nor the polymer overlayer are beneficial to the device performance. We thus believe even higher performance could be obtained from the BTTP-F/PCBM system through better control of vertical and lateral film morphology.

METHODS

Devices were fabricated in a planar configuration: glass/ITO/PEDOT:PSS/BTTP-F:PCBM/LiF/Al. ITO substrates (Colorado Concept Coatings) were cleaned by stepwise sonication in detergent, DI water, acetone, and IPA followed by 10 min of O_2 plasma etching. Filtered PEDOT/PSS (Baytron P VP Al 4083) was spun on the ITO substrates at 4 krpm for 30 s and annealed at 120 °C for 1 h to yield 40 nm thick films. PCBM was purchased from American Dye Source, and BTTP-F was synthesized by Suzuki coupling polymerization according to Zhu and Jenekhe.[26] All BTTP-F/PCBM solutions were prepared with anhydrous $CHCl_3$ (15 mg/mL). Solutions were heated and stirred at 55 °C to dissolve the constituents and filtered through 0.45 μm PTFE filters. The polymer solutions were spun in a N_2 glovebox at 0.8 krpm for 60 s, resulting in 180 nm films. Solvent vapor annealing of the BTTP-F/PCBM films was performed in enclosed glass Petri dishes in the glovebox. Samples were taped to the top of a Petri dish, and 5 mL of degassed chlorobenzene was added to the bottom. Cathodes of 1.0 nm of LiF and 80 nm of Al were deposited at 2×10^{-6} Torr, defining 3.14×10^{-2} cm^2 active areas.

All bulk solar cell measurements were performed in air using a 450 W Xe lamp and AM1.5 filter at 100 mW/cm^2 calibrated to an NREL certified silicon reference diode. The spectral irradiance of the light source and the responsivity of the reference cell were measured and used to calculate the spectral mismatch. Ten to 20 devices were averaged to obtain the results. External quantum efficiencies were measured using an Optronic Laboratories OL 750D double monochromator with a beam size of 1 mm. Photocurrents were recorded by a Keithly 2400 source meter in reference to a Si diode.

Hole-only SCLC devices were fabricated according to the above procedure with a 50 nm Au cathode in place of LiF/Al. The average BTTP-F/PCBM blend thickness was 180−200 nm. $I-V$ characteristics were measured with a Keithly 2400 source meter under an 8 mTorr vacuum.

Optical images were taken with a CCD through a Zeiss axiovert optical microscope. A Philips EM420 TEM was used to characterize the PCBM crystallites at a 100 kV accelerating voltage. All XPS spectra were taken on a Surface Science Instruments X-probe spectrometer at less than 5×10^{-9} Torr. X-ray spot size was on the order of 800 mm. Pass energy for survey spectra and detail scans of C, O, N, S, and Si (composition) was 150 eV. Angle-dependent data were acquired by varying the takeoff angle between the sample normal and the input axis of the energy analyzer. This allows for determining the composition of the sample at various sampling depths (0° take off angle at 80−100 Å, 55° take off angle at 50 Å, 80° take off angle at 20 Å).

The Service Physics ESCA 2000AGraphics Viewer program was used to determine peak areas and to calculate the elemental compositions from those peaks. Depth profile calculations were performed using an algorithm developed by Tyler and Ratner.[60,65] The mean free path of the emitted photoelectron used for the calculation was C = 36 Å, O = 32 Å, N = 35 Å, S = 38 Å, and Si = 39 Å. A smoothing factor was chosen to optimize the output data.

AFM measurements were performed using an Asylum Research MFP-3D AFM mounted on an inverted optical microscope as described in detail elsewhere.[47] A 2 mW, 632 nm HeNe laser excitation source was used for all illuminated measurements. LBIC was performed illuminating through the anode while using the AFM and optical setup. The scanner stage of the Asylum AFM is used for $x-y$ translation, the sample is enclosed in a fluid cell (N_2 environment), and the macroscopic cathode of the device is connected to the current preamplifier built into the AFM head *via* a 4 mil wire to monitor the current flow. The laser is focused to a diffraction limited spot, and neutral density filters are used to attenuate the intensity of the spot to 10 W/cm^2. Correlating the stage position with the current signal from the c-AFM head generates spatial maps, and spectroscopic data can be gathered at a fixed location by fixing the stage. The AFM tip is not used during LBIC experiments, so no topographical features are imaged.

Acknowledgment. Y. Zhu for initial synthesis of the copolymer under investigation, A.C. Young for help with phase contrast imaging, and A. K.-Y. Jen for use of his glovebox are gratefully acknowledged. L.S.C.P. acknowledges the support of the NSF Discovery Corps fellowship program (CHE 0725139). This study is supported by the STC Program of the National Science Foundation (DMR 0120967) and the NSF Career Award (DMR 0747489). D.S.G. acknowledges the support of the NSF (DMR-0120967 and DMR-0449422) as well as the DOE and AFOSR. D.S.G. is grateful for the support of the Camille Dreyfus Teacher-Scholar Awards Program, Cottrell Scholarship program of the Research Corporation, and the Alfred P. Sloan Foundation Research Fellowship program. S.A.J. acknowledges support from DOE, Basic Energy Sciences (DE-FG02-07ER46467), the NSF (Grant DMR-0805259), and AFOSR EHSS-MURI (Grant FA9550-06-1-0326).

Supporting Information Available: External quantum efficiency measurements, additional optical images, TEM and XRD of the PCBM crystallites, and raw XPS results. Supplemental LBIC and AFM images are also provided. This material is available free of charge *via* the Internet at http://pubs.acs.org.

REFERENCES AND NOTES

1. Zhao, Y.; Xie, Z. Y.; Qu, Y.; Geng, Y. H.; Wang, L. X. Solvent-Vapor Treatment Induced Performance Enhancement of Poly(3-hexylthiophene): Methanofullerene Bulk-Heterojunction Photovoltaic Cells. *Appl. Phys. Lett.* **2007**, *90*, 0435041–0435043.
2. Li, G.; Shrotriya, V.; Huang, J. S.; Yao, Y.; Moriarty, T.; Emery, K.; Yang, Y. High-Efficiency Solution Processable Polymer Photovoltaic Cells by Self-Organization of Polymer Blends. *Nat. Mater.* **2005**, *4*, 864–868.
3. Gregg, B. A. Evolution of Photophysical and Photovoltaic Properties of Perylene Bis(phenethylimide) Films upon Solvent Vapor Annealing. *J. Phys. Chem.* **1996**, *100*, 852–859.
4. Lloyd, M. T.; Mayer, A. C.; Subramanian, S.; Mourey, D. A.; Herman, D. J.; Bapat, A. V.; Anthony, J. E.; Malliaras, G. G. Efficient Solution-Processed Photovoltaic Cells Based on an Anthradithiophene/Fullerene Blend. *J. Am. Chem. Soc.* **2007**, *129*, 9144–9149.
5. McNeill, C. R.; Dastoor, P. C. Photocurrent Pattern Formation in Polymer/Methanofullerene Blends Imaged by Near-Field Scanning Photocurrent Microscopy. *J. Appl. Phys.* **2006**, *99*, 0335021–0335027.
6. Quist, P. A. C.; Martens, T.; Manca, J. V.; Savenije, T. J.; Siebbeles, L. D. A. Photo-Induced Charge Separation and Electron Diffusion in MDMO-PPV:PCBM Bulk Heterojunctions. *Sol. Energy Mater. Sol. Cells* **2006**, *90*, 362–378.
7. van Duren, J. K. J.; Yang, X.; Loos, J.; Bulle-Lieuwma, C. W. T.; Sieval, A. B.; Hummelen, J. C.; Janssen, R. A. J. Relating the Morphology of Poly(*p*-phenylene vinylene)/Methanofullerene Blends to Solar-Cell Performance. *Adv. Funct. Mater.* **2004**, *14*, 425–434.
8. Shaheen, S. E.; Ginley, D. S.; Jabbour, G. E. Organic-Based Photovoltaics: Toward Low-Cost Power Generation. *Mater. Res. Bull.* **2005**, *30*, 10–19.
9. Dennler, G.; Sariciftci, N. S. Flexible Conjugated Polymer-Based Plastic Solar Cells: From Basics to Applications. *P. IEEE* **2005**, *93*, 1429–1439.
10. Coakley, K. M.; McGehee, M. D. Conjugated Polymer Photovoltaic Cells. *Chem. Mater.* **2004**, *16*, 4533–4542.
11. Thompson, B. C.; Frechet, J. M. J. Polymer-Fullerene Composite Solar Cells. *Angew. Chem., Int. Ed.* **2008**, *47*, 58–77.
12. Gregg, B. A.; Mark, C. H. Comparing Organic to Inorganic Photovoltaic Cells: Theory, Experiment and Simulation. *J. Appl. Phys.* **2003**, *93*, 3605–3614.
13. Plextronics (August 9, 2007). Plextronics' Organic Solar Cell Technology Breaks World Record: National Renewable Energy Laboratory Certifies Cell Efficiency. Press Release. Retrieved on July 14, 2008.
14. Kim, J. Y.; Lee, K.; Coates, N. E.; Moses, D.; Nguyen, T. Q.; Dante, M.; Heeger, A. J. Efficient Tandem Polymer Solar Cells Fabricated by All-Solution Processing. *Science* **2007**, *317*, 222–225.
15. Hoppe, H.; Sariciftci, N. S. Organic Solar Cells: An Overview. *J. Mater. Res.* **2004**, *19*, 1924–1945.
16. Hoppe, H.; Sariciftci, N. S. Morphology of Polymer/Fullerene Bulk Heterojunction Solar Cells. *J. Mater. Chem.* **2006**, *16*, 45–61.
17. Xin, H.; Kim, F. S.; Jenekhe, S. A. Highly Efficient Solar Cells Based on Poly(3-butylthiophene) Nanowires. *J. Am. Chem. Soc.* **2008**, *130*, 5424–5425.
18. Ma, W. L.; Yang, C. Y.; Gong, X.; Lee, K.; Heeger, A. J. Thermally Stable, Efficient Polymer Solar Cells with Nanoscale Control of the Interpenetrating Network Morphology. *Adv. Funct. Mater.* **2005**, *15*, 1617–1622.
19. Reyes-Reyes, M.; Kim, K.; Carroll, D. L. High-Efficiency Photovoltaic Devices Based on Annealed Poly(3-hexylthiophene) and 1-(3-Methoxycarbonyl)-propyl-1-phenyl-(6,6)C-61 Blends. *Appl. Phys. Lett.* **2005**, *87*, 0835061–0835063.
20. Scharber, M. C.; Mühlbacher, D.; Koppe, M.; Denk, P.; Waldauf, C.; Heeger, A. J.; Brabec, C. J. Design Rules for Donors in Bulk-Heterojunction Solar Cells—Towards 10% Energy-Conversion Efficiency. *Adv. Mater.* **2006**, *18*, 789–794.
21. Andersson, M. R. Design, Synthesis and Properties of Low Band Gap Polyflourenes for Photovoltaic Devices. *Synth. Met.* **2005**, *154*, 53–56.
22. Andersson, M. R.; Inganas, O. High-Performance Polymer Solar Cells of an Alternating Polyfluorene Copolymer and Fullerene Derivative. *Adv. Mater.* **2003**, *15*, 988–991.
23. Andersson, M. R.; Inganas, O. New Low Band Gap Alternating Polyfluorene Copolymer-Based Photovoltaic Cells. *Sol. Energy Mater. Sol. Cells* **2007**, *91*, 1010–1018.
24. Inganas, O.; Andersson, M. R. Low-Bandgap Alternating Fluorene Copolymer/Methanofullerene Heterojunctions in Efficient Near-Infrared Polymer Solar Cells. *Adv. Mater.* **2006**, *18*, 2169–2173.
25. Winder, C.; Sariciftci, N. S. Low Bandgap Polymers for Photon Harvesting in Bulk Heterojunction Solar Cells. *J. Mater. Chem.* **2004**, *14*, 1077–1086.
26. Zhu, Y.; Champion, R. D.; Jenekhe, S. A. Conjugated Donor−Acceptor Copolymer Semiconductors with Large Intramolecular Charge Transfer: Synthesis, Optical Properties, Electrochemistry, and Field Effect Carrier Mobility of Thienopyrazine-Based Copolymers. *Macromolecules* **2006**, *39*, 8712–8719.
27. Yang, X.; Loos, J.; Veenstra, S. C.; Verhees, W. J. H.; Wienk, M. M.; Kroon, J. M.; Michels, M. A. J.; Janssen, R. A. J. Nanoscale Morphology of High-Performance Polymer Solar Cells. *Nano Lett.* **2005**, *5*, 579–583.
28. Katz, E. A.; Faiman, D.; Tuladhar, S. M.; Kroon, J. M.; Wienk, M. M.; Fromherz, T.; Padinger, F.; Brabec, C. J.; Sariciftci, N. S. Temperature Dependence for the Photovoltaic Device Parameters of Polymer-Fullerene Solar Cells under Operating Conditions. *J. Appl. Phys.* **2001**, *90*, 5343–5350.
29. Yang, X.; Duren, J. K. J. v.; Janssen, R. A. J.; Michels, M. A. J.; Loos, J. Morphology and Thermal Stability of the Active Layer in Poly(*p*-phenylenevinylene)/Methanofullerene Plastic Photovoltaic Devices. *Macromolecules* **2004**, *37*, 151–2158.
30. Nilsson, S.; Bernasik, A.; Budkowski, A.; Moons, E. Morphology and Phase Segregation of Spin-Casted Films of Polyfluorene/PCBM Blends. *Macromolecules* **2007**, *40*, 8291–8301.
31. Zhong, H. F.; Yang, X. N.; deWith, B.; Loos, J. Quantitative Insight into Morphology Evolution of Thin PPV/PCBM

Composite Films upon Thermal Treatment. *Macromolecules* **2006**, *39*, 218–223.

32. Campoy-Quiles, M.; Ferenczi, T.; Agostinelli, T.; Etchegoin, P. G.; Kim, Y.; Anthopoulos, T. D.; Stavrinou, P. N.; Bradley, D. D. C.; Nelson, J. Morphology Evolution *via* Self-Organization and Lateral and Vertical Diffusion in Polymer:Fullerene Solar Cell Blends. *Nat. Mater.* **2008**, *7*, 158–164.
33. Marek, J. Light-Beam-Induced Current Characterization of Grain Boundaries. *J. Appl. Phys.* **1984**, *55*, 318–326.
34. Redfield, D. Silicon-Silicon Interfaces. *Appl. Phys. Lett.* **1982**, *40*, 163–165.
35. Rinio, M.; Moller, H. J.; Werner, M. LBIC Investigations of the Lifetime Degradation by Extended Defects in Multicrystalline Solar Silicon. *Solid State Phenom.* **1998**, *63−64*, 115–122.
36. Stemmer, M.; Martinuzzi, S. *Minority-Carrier Diffusion Length Mapping of Extended Crystallographic Defects in Semiconductor Silicon*; Jimenez, J., Ed.; IOP Publishing Ltd.: 1994; pp 239−242.
37. Warta, W. Defect and Impurity Diagnostics and Process Monitoring. *Sol. Energy Mater. Sol. Cells* **2002**, *72*, 389–401.
38. Liau, Y. H.; Scherer, N. F.; Rhodes, K. Nanoscale Electrical Conductivity and Surface Spectroscopic Studies of Indium-Tin Oxide. *J. Phys. Chem. B* **2001**, *105*, 3282–3288.
39. Lin, H. N.; Lin, H. L.; Wang, S. S.; Yu, L. S.; Perng, G. Y.; Chen, S. A.; Chen, S. H. Nanoscale Charge Transport in an Electroluminescent Polymer Investigated by Conducting Atomic Force Microscopy. *Appl. Phys. Lett.* **2002**, *81*, 2572–2574.
40. Paul, S.; Kanwal, A.; Chhowalla, M. Memory Effect in Thin Films of Insulating Polymer and C-60 Nanocomposites. *Nanotechnology* **2006**, *17*, 145–151.
41. Pingree, L. S. C.; Hersam, M. C.; Kern, M. M.; Scott, B. J.; Marks, T. J. Spatially-Resolved Electroluminescence of Operating Organic Light-Emitting Diodes Using Conductive Atomic Force Microscopy. *Appl. Phys. Lett.* **2004**, *85*, 344–346.
42. Hersam, M. C.; Hoole, A. C. F.; O'Shea, S. J.; Welland, M. E. Potentiometry and Repair of Electrically Stressed Nanowires Using Atomic Force Microscopy. *Appl. Phys. Lett.* **1998**, *72*, 915–917.
43. Alexeev, A.; Loos, J.; Koetse, M. M. Nanoscale Electrical Characterization of Semiconducting Polymer Blends by Conductive Atomic Force Microscopy (C-AFM). *Ultramicroscopy* **2006**, *106*, 191–199.
44. Inonescu-Zanetti, C.; Mechler, A.; Carter, S. A.; Lal, R. Semiconductive Polymer Blends: Correlating Structure with Transport Properties at the Nanoscale. *Adv. Mater.* **2004**, *16*, 385–389.
45. Pingree, L. S. C.; MacLeod, B. A.; Ginger, D. S. The Changing Face of PEDOT:PSS Films: Substrate, Bias, and Processing Effects on Vertical Charge Transport. *J. Phys. Chem. C* **2008**, *112*, 7922–7927.
46. Reid, O. G.; Munechika, K.; Ginger, D. S. Space Charge Limited Current Measurements on Conjugated Polymer Films Using Conductive Atomic Force Microscopy. *Nano Lett.* **2008**, *8*, 1602–1609.
47. Coffey, D. C.; Reid, O. G.; Rodovsky, D. B.; Bartholomew, G. P.; Ginger, D. S. Mapping Local Photocurrents in Polymer/Fullerene Solar Cells with Photoconductive Atomic Force Microscopy. *Nano Lett.* **2007**, *7*, 738–744.
48. Shrotriya, V.; Li, G.; Yao, Y.; Moriarty, T.; Emery, K.; Yang, Y. Accurate Measurement and Characterization of Organic Solar Cells. *Adv. Funct. Mater.* **2006**, *16*, 2016–2023.
49. Pacios, R.; Bradley, D. D. C.; Nelson, J.; Brabec, C. J. Efficient Polyflourene Based Solar Cells. *Synth. Met.* **2003**, *137*, 1469–1470.
50. Yang, X.; van Duren, J. K. J.; Rispens, M. T.; Hummelen, J. C.; Janssen, R. A. J.; Michels, M. A. J.; Loos, J. Crystalline Organization of Methanofullerene as Used for Plastic Solar-Cell Applications. *Adv. Mater.* **2004**, *16*, 802–806.
51. Rispens, M. T.; Meetsma, A.; Rittberger, R.; Brabec, C. J.; Sariciftcib, N. S.; Hummelen, J. C. Influence of the Solvent on the Crystal Structure of PCBM and the Efficiency of MDMO-PPV:PCBM 'Plastic' Solar Cells. *Chem. Commun.* **2003**, *17*, 2116–2118.
52. Savenije, T.; Kroeze, J.; Yang, X.; Loos, J. The Effect of Thermal Treatment on the Morphology and Charge Carrier Dynamics in a Polythiophene-Fullerene Bulk Heterojunction. *Adv. Funct. Mater.* **2005**, *15*, 1260–1266.
53. McNeill, C. R.; Halls, J. J. M.; Wilson, R.; Whiting, G. L.; Berkebile, S.; Ramsey, M. G.; Friend, R. H.; Greenham, N. C. Efficient Polythiophene/Polyfluorene Copolymer Bulk Heterojunction Photovoltaic Devices: Device Physics and Annealing Effects. *Adv. Funct. Mater.* **2008**, *18*, 2309–2321.
54. Sharma, G. D.; Choudhary, V. S.; Roy, M. S. Effect of Annealing on the Optical, Electrical, and Photovoltaic Properties of Bulk Hetero-Junction Device Based on PPAT:TY Blend. *Sol. Energy Mater. Sol. Cells* **2007**, *91*, 275–284.
55. Lampert, M. A.; Mark, P. *Current Injection in Solids*; Academic Press: New York, 1970; p 354.
56. Schauer, F. Space-Charge-Limited Currents for Organic Solar Cell Optimisation. *Sol. Energy Mater. Sol. Cells* **2005**, *87*, 235–250.
57. Jain, S. C.; Geens, W.; Mehra, A.; Kumar, V.; Aernouts, T.; Poortmans, J.; Mertens, R.; Willander, M. Injection- and Space Charge Limited-Currents in Doped Conducting Organic Materials. *J. Appl. Phys.* **2001**, *89*, 3804–3810.
58. Skotheim, T. A.; Reynolds, J. R. *Handbook of Conducting Polymers*; Marcel Dekker: New York, 2007; Vol. 2, p 1680.
59. Dante, M.; Peet, J.; Nguyen, T.-Q. Nanoscale Charge Transport and Internal Structure of Bulk Heterojunction Conjugated Polymer/Fullerene Solar Cells by Scanning Probe Microscopy. *J. Phys. Chem. C* **2008**, *112*, 7241–7249.
60. Tyler, B.; Castner, D.; Ratner, B. Regularization: A Stable and Accurate Method for Generating Depth Profiles from Angle-Dependent XPS Data. *Surf. Interface Anal.* **1989**, *14*, 443–450.
61. Bjorstrom, C. M.; Nilsson, S.; Bernasik, A.; Budkowski, A.; Andersson, M.; Magnusson, K. O.; Moons, E. Vertical Phase Separation in Spin-Coated Films of a Low Bandgap Polyfluorene/PCBM Blend: Effects of Specific Substrate Interaction. *Appl. Surf. Sci.* **2007**, *253*, 3906–3912.
62. Coffey, D. C.; Ginger, D. S. Patterning Phase Separation in Polymer Films with Dip-Pen Nanolithography. *J. Am. Chem. Soc.* **2005**, *127*, 4564–4565.
63. Park, L. Y.; Munro, A. M.; Ginger, D. S. Controlling Film Morphology in Conjugated Polymer:Fullerene Blends with Surface Patterning. *J. Am. Chem. Soc.* **2008**, *130*, 15916–15926.
64. Wei, J. H.; Coffey, D. C.; Ginger, D. S. Nucleating Pattern Formation in Spin Coated Polymer Blend Films with Nanoscale Surface Templates. *J. Phys. Chem. B* **2006**, *110*, 24324–24330.
65. Tyler, B.; Castner, D.; Ratner, B. Determining Depth Profiles from Angle Dependent XPS: The Effects of Analyzer Lens Aperture Size and Geometry. *J. Vac. Sci. Technol., A* **1989**, *7*, 1646–1654.